5-2020

Characterizing Plasma with Emission Tomography-Feasibility Study on Synthetic and Experimental Data

M. Nikolić

A. Samolov

A. Godunov

L. Vušković,

S. Popović

Review of Scientific Instruments

Characterizing plasma with emission tomography—Feasibility study on synthetic and experimental data

Cite as: Rev. Sci. Instrum. **91**, 053102 (2020); https://doi.org/10.1063/1.5138921
Submitted: 15 November 2019 . Accepted: 08 April 2020 . Published Online: 05 May 2020

M. Nikolić, A. Samolov, A. Godunov, L. Vušković, and S. Popović

AIP Publishing

Review of Scientific Instruments ARTICLE scitation.org/journal/rsi

Characterizing plasma with emission tomography—Feasibility study on synthetic and experimental data

Cite as: Rev. Sci. Instrum. 91, 053102 (2020); doi: 10.1063/1.5138921
Submitted: 15 November 2019 • Accepted: 8 April 2020 •
Published Online: 5 May 2020

M. Nikolić,[1,a] A. Samolov,[2] A. Godunov,[3] L. Vušković,[3] and S. Popović[3]

AFFILIATIONS

[1] Department of Physics and Astronomy, University of San Francisco, San Francisco, California 94117, USA
[2] Varian Semiconductor Equipment, Silicon Systems Group, Applied Materials, Gloucester, Massachusetts 01930, USA
[3] Department of Physics, Center for Accelerator Science, Old Dominion University, Norfolk, Virginia 23529, USA

[a] **Author to whom correspondence should be addressed:** mnikolic@usfca.edu

ABSTRACT

We present a feasibility study on different tomographic algorithms to overcome the issues of finite sets of projection data, limited viewing angles, and noisy data, which cause the tomographic reconstruction to be an ill-posed inversion problem. We investigated three approaches: single angle Abel inversion, two angle approach, and multiple angle 2D plasma tomography. These methods were tested on symmetric and asymmetric sample functions and on experimental results from a supersonic flowing argon microwave plasma sustained in a cylindrical quartz cavity. The analysis focused on the afterglow region of the microwave flow where a plasmoid-like formation was observed. We investigated the effects of the uniform random noise added to the simulated data by applying smoothing techniques. The quality of reconstructed images was assessed by using peak signal-to-noise ratio and universal quality image measures. The results showed that the Abel inversion approach could be employed only when the system is radially symmetric, while the systems with slight asymmetry could be reconstructed with the two angle approach. In the complete absence of symmetry, full 2D tomographic reconstruction should be applied. The data analysis showed that the best results were obtained by employing either the filtered back projection or the simultaneous algebraic reconstruction technique. The total variation minimization method proved to be the best denoising technique. Each approach was used to obtain the spatial distributions of argon excited states taken at three positions along the plasmoid-like structure. The results indicated that the plasma was asymmetric with argon populating the cavity surface.

I. INTRODUCTION

The importance of understanding and characterizing the main plasma parameters has been a focal point of academic and industrial research for decades.[1,2] Various experimental and numerical methods have been developed in an attempt to fully describe dynamics of gas discharges.[3–6] Often it is necessary to apply non-intrusive and *in situ* measurement techniques. Optical emission and absorption spectroscopy represent primary tools in achieving these goals since they allow direct and indirect measurements of fundamental plasma parameters, such as velocities, temperatures, and population densities.[7–12] However, these optical techniques provide only insight into integrated effects of collective plasma behavior. In order to look into the internal dynamics of the discharge, the integrated data need to be transformed into the spatial distributions. A commonly used method for reconstruction of an inner plasma structure is the Abel inversion, which assumes radial symmetry of the plasma configuration.[13–18] However, Abel inversion is not applicable in the case of non-stationary, inhomogeneous plasmas with strong radial asymmetry. It follows that the discharge should be observed from at least two angles of observation. One way to obtain spatial distributions of various emitters in the plasma is to employ plasma tomography methods based on observing the discharge at several projections distributed at different viewing angles.[19] The idea to employ tomography as a tool for solving physics problems has long been present in both theoretical and numerical research fields.[19–23]

However, implementing the tomography methods for specific problems represents a challenge due to the limited number of data and views in plasma. Over the years, extensive studies have been conducted to develop a simplified method where only two mutually perpendicular directions were used to obtain the inner plasma structure.[24,25] This approximation includes only the first two terms in the Fourier transform of the Radon integral, making it difficult to depict the entire angular distribution of plasma parameters. Therefore, whenever possible, a full two-dimensional tomography, where the plasma is observed at multiple viewing projections and angles, should be applied. A number of valuable approaches were developed for tomographic reconstruction and are available in the literature. The commonly used reconstruction algorithms belong to three main groups: analytical methods [such as Filtered Back Projection (FBP)[26,27] and GRIDREC[28,29]], algebraic methods [such as Algebraic Reconstruction Technique (ART) and Simultaneous Algebraic Reconstruction Technique (SIRT)],[26,30] and statistical methods (such as maximum likelihood method).[31,32]

One of the main issues when applying reconstruction techniques to experimental data is the limited number of viewing projections and the presence of noise. Over the years, numerous interpolation (i.e., Lagrange interpolation and cubic spline approximation) and smoothing [i.e., moving average filter,[33] non-local means algorithm,[34,35] and total variation (TV) minimization[36,37]] techniques were developed to overcome this problem. Specifically, the techniques based on the Tikhonov problem formulation proved to be highly successful in the case of the sparse data where some prior information is known.[38–41]

In this study, we evaluated the applicability of all reconstruction techniques discussed above (Abel inversion, two angle approach, and 2D tomography) for their use in plasmas with the cylindrical geometry. The tomographic methods were tested with three different testing functions. To simulate experimental conditions, a random uniform noise of 1%, 5%, and 10% was added to theoretical values generated from the testing functions. We estimated the quality of the reconstructed images by employing two well-known measures: universal image quality index (UQI)[42] and peak signal-to-noise ratio (PSNR).

We employed the proposed inversion techniques to evaluate spatial population distributions of the neutral argon excited state $\left[3s^2 3p^5 (^2P^0_{1/2}) 4p, J = 1\right]$ obtained from the spectral line intensity at 714.70 nm. Argon plasma was generated inside a microwave supersonic flowing cavity with the inner diameter of 32 mm.[43] The experimental setup only allowed measurements at 21 viewing angles in the range of 46°–168° with 17 viewing projections. Reconstruction algorithms were tested based on these constraints.

In Secs. II–IV, we briefly describe these approaches to improve data stability and to estimate the quality of the reconstructed images. Then we provide the detailed description of the proposed inversion techniques and discuss their applicability (Sec. V). Finally, we present and discuss the experimental results (Sec. VI).

II. RADON TRANSFORM

Currently, the image reconstruction in many research fields is based on the application of a Radon transform integral.[19] The Radon transform is an integral transform whose inverse offers a means of determining the total density of a certain function along a line, L. To illustrate this, let us start by looking at light leaving plasma at an angle θ with respect to the x-axis of the coordinate system outlined in Fig. 1. To better visualize the problem, it is useful to transfer to new coordinates s and p that are rotated by the given angle θ with respect to x and y coordinates. Then,

$$s = x\cos\theta + y\sin\theta, \tag{1}$$

$$p = -x\sin\theta + y\cos\theta. \tag{2}$$

Figure 1 shows that the total light intensity, $I(p, \theta)$, emitted from the plasma at an angle θ and distance p from the center of the plasma represents the sum of light intensities from all plasma emitters, aligned along a line parallel to the s-axis. This effect was studied by Radon[19] who showed that for a large number of emitters, the sum of line intensities becomes the line integral, also called a Radon integral,

$$I(p,\theta) = \Re[\varepsilon(x,y)] = \int_L \varepsilon(x,y)\,ds, \tag{3}$$

where L is the line of integration, ds is the increment of the length along that line, and $\varepsilon(x, y)$ is a two-dimensional emissivity function of the plasma.

Radon theorem asserts that if intensities, $I(p, \theta)$, along every projection, p, and over all directions, θ, are known, then the inverse Radon integral exists and the emissivity function can be uniquely reconstructed from $I(p, \theta)$,

$$\varepsilon(x,y) = \Re^{-1}[I(p,\theta)]. \tag{4}$$

However, in plasma physics, the number of projection intensities together with the number of available viewing angles is often limited due to the complexity of the experimental and diagnostic systems. Specifically, in the case of low-pressure plasma systems, where the plasma is generated in vacuum chambers, the number of viewing angles is limited mostly by the available optical access (i.e., the presence of windows on the usually opaque chamber walls). From the mathematical point of view, the problem of plasma reconstruction is a highly ill-posed problem. Furthermore, the experimental projection data are almost always disturbed by the presence of noise. This means that there exists an infinite number of functions

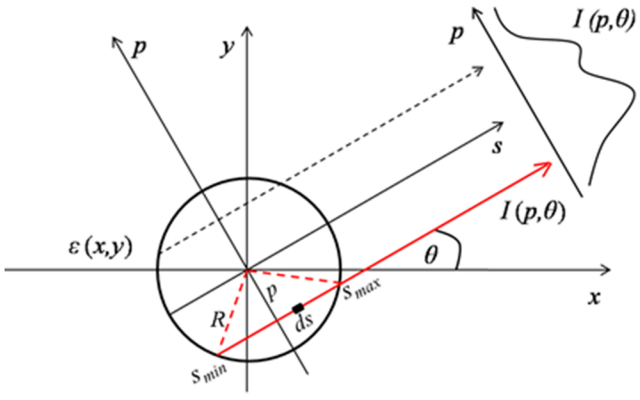

FIG. 1. Parallel beam projection scheme at a specific angle.

$\varepsilon(x, y)$ that satisfy Eq. (3) within the experimental error. Therefore, it is crucial to increase the stability and precision of the reconstruction techniques by smoothing and interpolating the limited experimental data and providing alternate solutions when the number of viewing angles is limited.

III. DATA STABILITY

In practical applications, projections are measured as a discrete set of experimental data points. In order to provide a larger number of projections and obtain smoothing of the existing data, various interpolation techniques are usually applied. The commonly used techniques, such as Lagrange interpolation and cubic spline approximation, belong to a family of functions that is based on the spatial domain filtering. In the case when *a priori* information about the smoothness of the experimental data exists, it is beneficial to employ smoothing functions based on moving average filters.[33] A moving average filter smooths the data by replacing each data point with the average of the neighboring data points defined within the span and is given with the following equation:

$$y_s(i) = \frac{y(i+N) + y(i+N-1) + \cdots + y(i-N)}{2N+1}, \tag{5}$$

where $y_s(i)$ is the smoothed value for the i-th data point, N is the number of neighboring data points on either side of $y_s(i)$, and $2N + 1$ is the number of data points. Currently, the widely used approach is a non-local algorithm for image denoising.[34,35] In this algorithm, the image is divided into i pixels with a value $I(i)$ of each pixel. The image is then scanned in search of all pixels that really resemble the pixel that needs to be denoised. The estimate value $\hat{I}(i)$ is computed based on the weighted average of all the pixels j on the image,

$$\hat{I}(i) = \sum_j \omega_{ij} I(j), \tag{6}$$

where the family of weights ω_{ij} depends on the similarity between the pixels i and j and is determined as

$$\omega_{ij} = \frac{1}{Z_i} e^{-\frac{G_d * |I(N^d(i)) - I(N^d(j))|^2}{h^2}}. \tag{7}$$

The constant $Z_i = \sum_j \omega_{ij}$ is a normalizing term, G_d is a Gaussian spatial kernel, $I(N^d(i)) - I(N^d(j))$ is an Euclidean distance between the neighborhoods $N^d(i)$ and $N^d(j)$ of the gradient orientation at pixels x_i and x_j, and h acts as a filtering parameter. The filtering parameter controls the decay of the exponential function and therefore the decay of the weights as a function of the Euclidean distances. This parameter is typically adjusted manually in the algorithm.

The general approach when reconstructing noisy data with a limited number of angles is to apply different regularization methods developed by Tikhonov.[38,39] These methods designate the family of algorithms that adjust the values of the pixels in the reconstructed image until its projections resemble most closely the measured ones. The solution, however, is not unique, and it is necessary to establish *a priori* criteria for its convergence. Various theoretical approaches have been developed in order utilize the Tikhonov approach for plasma tomography out of which the most commonly used is total variation minimization.[36,37]

Total variation (TV) minimization is based on minimizing the norm of the discrete gradient (i.e., total variation) of the reconstructed image. The goal is to find the solution to the reconstruction problem that has the lowest total variation. This can be achieved by applying the well-known steepest descent method given by the iterative relation

$$\varepsilon_{k+1} = \varepsilon_k - \lambda \nabla TV\,|_{\varepsilon_k}, \tag{8}$$

where ∇TV is the gradient of the total variation of the given function and λ is the regularization parameter.

The role of the regularization parameter, λ, is to regulate relative weights between the prior information and the noisy data. Estimating this parameter represents a very important step in the iterative algorithm. A very large λ provides a reconstruction where noise is suppressed, but some useful information about the resulting reconstruction may also be lost. An underestimation of λ leads to a case where both artifacts and noise will be present in the reconstruction. In practice, the regularization parameter is either adaptively selected for each iteration step or set as a constant that is estimated empirically.

In conclusion, when no *a priori* knowledge about the smoothness of the experimental data exists, it is beneficial to apply spatial domain filters. Spatial filters eliminate noise to a reasonable extent but at the cost of image blurring, which in turn loses sharp edges. When *a priori* information about the experimental data is available, it is recommended to employ either total variation or non-local regularization methods. Specifically, the total variation regularization has achieved great success in image denoising because it can not only effectively calculate the optimal solution but also retain sharp edges. However, in the case of very noisy data, even with good estimation of the regularization parameter λ, images tend to be over-smoothed, flat areas are approximated by a constant surface, resulting in a stair-case effect, and the image suffers from losses of contrast.[46] At present, most research on image denoising is focused on the adaptive algorithm based on combining non-local methods with total variation regularization. The results showed that the combination of these two models was successful in removing noise.[47] Nevertheless, structural information is not well preserved by these methods when noisy data are present, which degrades the visual image quality. This study will discuss the benefits of employing all techniques depending on the experimental system at hand.

IV. QUALITY OF RECONSTRUCTED IMAGES

Objective image quality measures play a very important role in tomographic image reconstruction. There are two classes of objective quality image assessment approaches. One is based on using the human visual system (HVS) characteristics to incorporate the perceptual quality measure.[45] The other class is mathematically defined measures such as the widely used mean squared error (MSE) and the peak signal-to-noise ratio (PSNR) but also the less popular universal image quality index (UQI).[42] The mean squared error (MSE) between two signals x and y is given as

$$MSE(x, y) = \frac{1}{N} \sum_{i=1}^{N} (x_i - y_i)^2. \tag{9}$$

One issue with the MSE is that it depends strongly on the image intensity scaling. A 10-bit image with a MSE of 100.0 looks much better than an 8-bit image with the same MSE. This is why the MSE is usually expressed as the peak signal-to-noise ratio (PSNR) as

$$PSNR = 10 \log_{10} \frac{L^2}{MSE}, \tag{10}$$

where L is the dynamic range of allowable pixel intensities. The PSNR is a useful tool when comparing restoration results for the same image, but the reconstruction quality of different images cannot be compared using this method.

Unlike MSE and PSNR methods that use error summation methods, the universal image quality index (UQI) is based on three factors: loss of correlation, luminance distortion, and contrast distortion. It also does not depend on the reconstructed images, the viewing conditions, or the individual observers. Therefore, it can provide a meaningful comparison between various types of images.

In this study, we used both the PSNR and the UQI method to obtain the quality of the reconstructed test images.

V. INVERSION TECHNIQUES

As already stated, tomographic reconstruction of noisy data with a limited number of projections and viewing angles still presents a challenge for the scientific community. Due to the complexity of the modern experimental systems, it is often difficult to observe the plasma from every angle. Therefore, it is very useful when it is possible to reconstruct the inner structure of the plasma when only one or two observing angles are available. In Subsections V A–V C, we will discuss three approaches applicable for plasma reconstruction. The simplest approach is Abel inversion, possible only when the plasma is radially symmetric. The main advantage of this approach is that it allows measurements from only one viewing angle. In the case of asymmetric discharges, when only a small observation window is available, it is possible to obtain spatial distributions of plasma parameters by using two mutually perpendicular directions. However, if possible, the full two-dimensional plasma tomography on the 0°–180° angle range would provide the most accurate and stable data.

The validity of these approaches was tested on the examples of the Gaussian distribution function

$$f(x,y) = \exp(-x^2 - y^2) \tag{11}$$

and the two asymmetric sample functions

$$f(x,y) = x + 3y \tag{12}$$

and

$$f(x,y) = \left(1 - \frac{x}{2} + x^5 + y^3\right) \exp\left(-x^2 - y^2\right). \tag{13}$$

The Gaussian distribution function was chosen because it is radially symmetric and provides a good testing example for Abel inversion, while the asymmetric sample functions would show the applicability of the two angle approach. Since the first asymmetric sample function [Eq. (12)] deviates only slightly from the axial symmetry, we expect that employing the two angle approach would provide an accurate reconstruction of this function. On the other hand, using the second asymmetric sample function [Eq. (13)] will explore the limits of the two angle approach. Finally, we tested the sample asymmetry function [Eq. (13)] with 2D plasma tomography techniques to provide the information on the stability and overall precision of the applied methods.

To simulate the experimental conditions, all reconstructed images were presented on a circle with 32-mm diameter.

A. Abel inversion

The Abel transform represents a special case of Radon transform when the distribution function is radially symmetric and depends only on $r = \sqrt{x^2 + y^2}$, so $\varepsilon(x, y) = \varepsilon(r)$. This means that the set of projections $I(p, \theta)$ is equivalent for any angle θ. After these simplifications, the Radon integral given in Eq. (3) becomes

$$I(y) = 2 \int_0^\infty \varepsilon(r)\, dx = 2 \int_y^\infty \frac{\varepsilon(r) r dr}{\sqrt{r^2 - y^2}}, \tag{14}$$

where $x = \sqrt{r^2 - y^2}$ and $x\, dx = r\, dr$.

The inverse integral of Abel transform is the widely used formula in the literature,[19]

$$\varepsilon(r) = -\frac{1}{\pi} \int_r^\infty \frac{I'(y) dy}{\sqrt{y^2 - r^2}}, \tag{15}$$

where $I'(y)$ is the first derivative of $I(y)$ with respect to y.

Figure 2 shows a comparison between the original Gaussian distribution and the values of the same function obtained after performing direct and inverse Abel transforms. To mimic the real experimental conditions and to test the stability of the numerical codes, a random noise of 1%, 2%, 5%, and 10% was added to the projections obtained after the direct Abel integral.

As shown in Fig. 2, even at a random noise of 2%, it was hard to reconstruct the original function. However, when the reconstructed data were smoothed by applying the smoothing function [Eq. (5)]

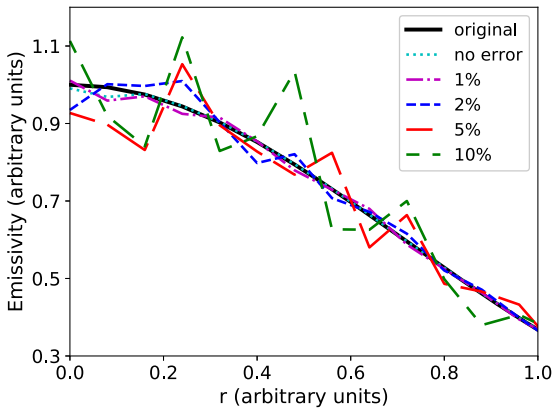

FIG. 2. The inverse Abel transform of the Gaussian distribution function and comparison between the original function and Gaussian profiles with no error, 1%, 2%, 5%, and 10% error.

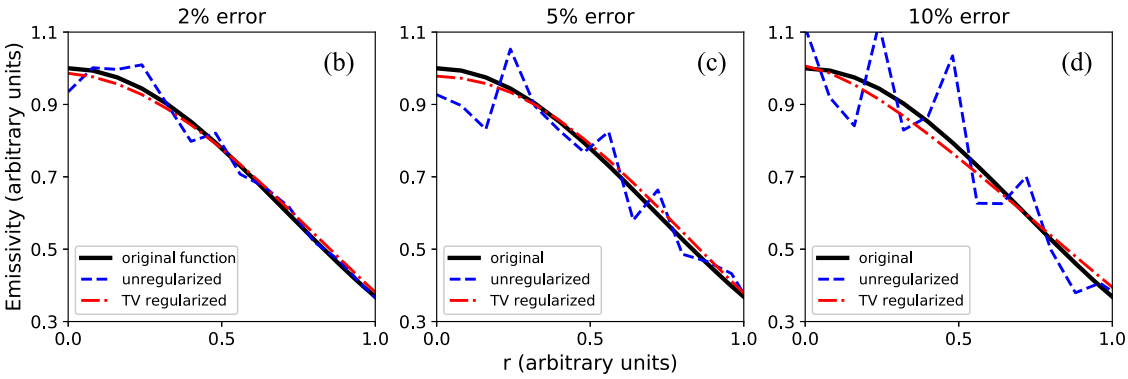

FIG. 3. The inverse Abel transform of the Gaussian distribution function and comparison between the original function and unregularized and regularized Gaussian profiles with (a) 2%, (b) 5%, and (c) 10% random noise.

and then regularized with the total variation (TV) minimization method [Eq. (8)], we were able to reproduce the original data even at a random noise of 10%. A comparison between the original Gaussian function and unregularized and regularized reconstruction at various noise levels (2%, 5%, and 10%) is presented in Fig. 3. The regularization parameter λ was chosen independently for each case. For low noise levels (1% and 2% noise), when the data were smooth, small values of λ (λ = 0.1–0.2) were used. On the other hand, large values of λ (λ = 0.5–0.9) were necessary to reconstruct noisy data (5% and 10% noise). The results in Fig. 3 show that with some *a priori* knowledge about the noise introduced into the experimental dataset, it is possible to fully reconstruct spatial distributions of atoms/molecules in the radially symmetric plasma.

To better visualize the effects of TV regularization, Fig. 4 shows a comparison between the original Gaussian function and unregularized and regularized Gaussian profiles with 10% random noise. We applied the universal image quality index (UQI) and peak signal-to-noise ratio (PSNR) to quantitatively measure the discrepancy between the original and reconstructed images. In the case of the unregularized reconstruction, PSNR = 25.41 dB and UQI = 0.89, while in the case of TV regularized reconstruction, PSNR = 35.48 dB and UQI = 0.996, where UQI = 1 would correspond to the perfect match.

Obviously, the Abel inversion approach is only meaningful if the system possesses radial symmetry. The Abel inversion method uses the data observed at only one direction and produces a 2D image that is always represented by a set of concentric circles. Thus, in the case of asymmetric systems [such as test functions given by Eqs. (12) and (13)], Abel inversion is not a good choice of the reconstruction method because the results depend highly on that one viewing angle chosen.

B. Two angle approach

Abel inversion represents a very useful tool for reconstruction of radially symmetric discharges, but in the case of radial asymmetry,

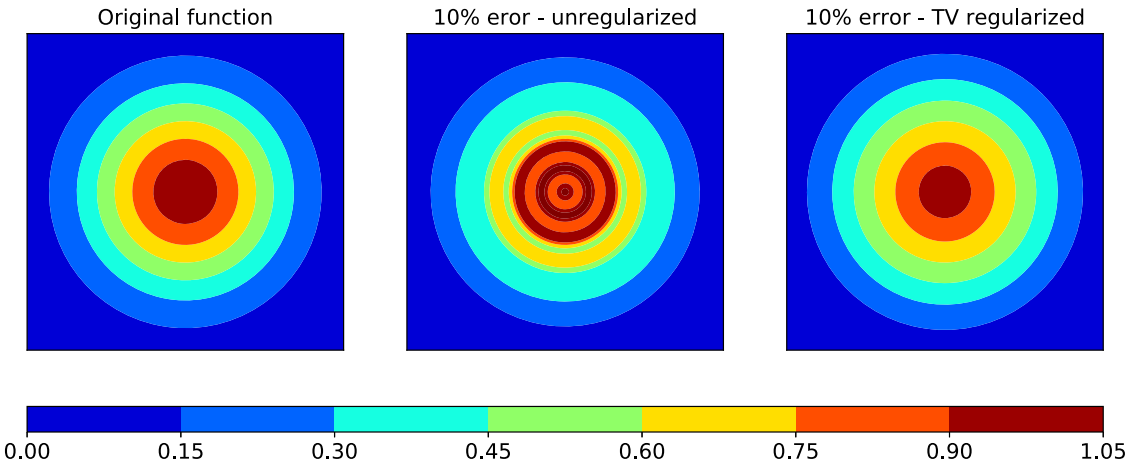

FIG. 4. 2D plot of the inverse Abel transform of the Gaussian distribution function and comparison between the original function and unregularized and regularized Gaussian profiles with 10% random noise.

two-dimensional plasma tomography with multiple viewing angles should be employed. However, due to the limited access to the plasma and due to the cost and complexity of the diagnostic systems, experimental setups often allow only two viewing directions. Over the years, multiple attempts with various degrees of success were achieved. In this work, we will discuss the approach to reconstruct the plasma emissivity function based on the measurements of spectral line intensities in two mutually perpendicular directions. This method is based on the assumption that the emissivity function is given by leading three terms in its Fourier expansion,[24,25]

$$\varepsilon(x,y) = \varepsilon(r,\theta) = H(r) + K(r)\cos\theta + L(r)\sin\theta, \tag{16}$$

where $H(r)$, $K(r)$, and $L(r)$ are monotonous functions of radius.

After applying above assumptions and combining Eq. (16) with Radon integral (3), we get

$$I(y) = \int_{x_{min}}^{x_{max}} (H(r) + K(r)\cos\theta + L(r)\sin\theta)\,dx,$$

$$I(x) = \int_{y_{min}}^{y_{max}} (H(r) + K(r)\cos\theta + L(r)\sin\theta)\,dy,$$

where $x_{max} = -x_{min} = \sqrt{R^2 - y^2}$, $y_{max} = -y_{min} = \sqrt{R^2 - x^2}$, $\cos\theta = x/r$, and $\sin\theta = y/r$.

By applying the symmetry properties of the sine and cosine functions on the symmetric interval within an angle θ interval $\left(-\frac{\pi}{2}, \frac{\pi}{2}\right)$ and combining the symmetric and asymmetric parts of the observed distributions, we derive

$$\begin{aligned} H(r) &= -\frac{1}{\pi}\int_r^R \left(\frac{I(x)+I(-x)}{2}\right)' \frac{dx}{\sqrt{x^2-r^2}}, \\ \frac{K(r)}{r} &= -\frac{1}{\pi}\int_r^R \left(\frac{I(x)-I(-x)}{2x}\right)' \frac{dx}{\sqrt{x^2-r^2}} \end{aligned} \tag{17}$$

and

$$\begin{aligned} H(r) &= -\frac{1}{\pi}\int_r^R \left(\frac{I(y)+I(-y)}{2}\right)' \frac{dy}{\sqrt{y^2-r^2}}, \\ \frac{L(r)}{r} &= -\frac{1}{\pi}\int_r^R \left(\frac{I(y)-I(-y)}{2y}\right)' \frac{dy}{\sqrt{y^2-r^2}}. \end{aligned} \tag{18}$$

Function $H(r)$ can be evaluated either from horizontal or vertical measurements, and this can serve as a good test of the applied technique.

Restricting the distribution to only three terms introduces greater probability for inhomogenities and phantom images to appear, which presents difficulties for formulating the entire angular distribution of plasma parameters. However, if the emissivity distribution shows only a small departure from the axial symmetry, this approach provides accurate reconstruction of the original function.[24,25] Therefore, having *a priori* information about the plasma system at hand represents a crucial step when choosing this reconstruction technique.

We have simulated the experimental measurement of spectral line intensities with the direct Radon integral, and the algorithm proved to have sufficient accuracy.[43] Then, we have employed the measurements at 0° and 90° to reconstruct the test functions.

A comparison between the original function, $\varepsilon(x, y) = x + 3y$, and the function reconstructed from the two path method when no error is introduced is given in Fig. 5. We applied the universal image quality index (UQI) and peak signal-to-noise ratio (PSNR) to quantitatively measure the discrepancy between the original and reconstructed images. In this case, UQI was equal to 0.97, where 1 corresponds to the perfect match.

Similarly, as in Sec. V A, to test the stability of the applied two path method, we introduced a random noise of 1%, 5%, and 10% to the projections after the direct Radon transform was performed. The reconstructions were smoothed by applying various smoothing filters described in Sec. III. The best results were obtained when using the non-local means (NL-means) algorithm and the total variation minimization (TV) method.

Figure 6 shows the comparison between the reconstruction images. The regularization parameter λ was chosen independently

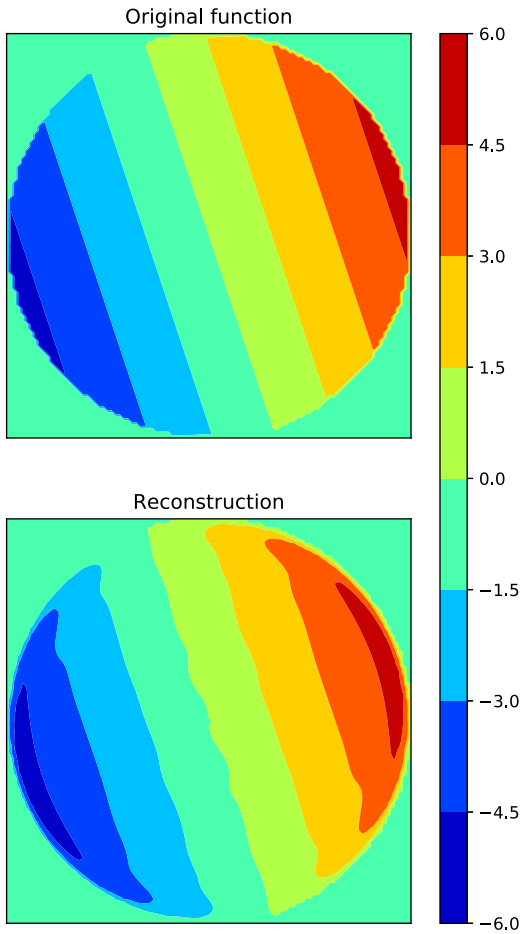

FIG. 5. Emissivity reconstruction for asymmetric discharge, represented by $\varepsilon(x, y) = x + 3y$, UQI = 0.97, and PSNR = 9.46 dB.

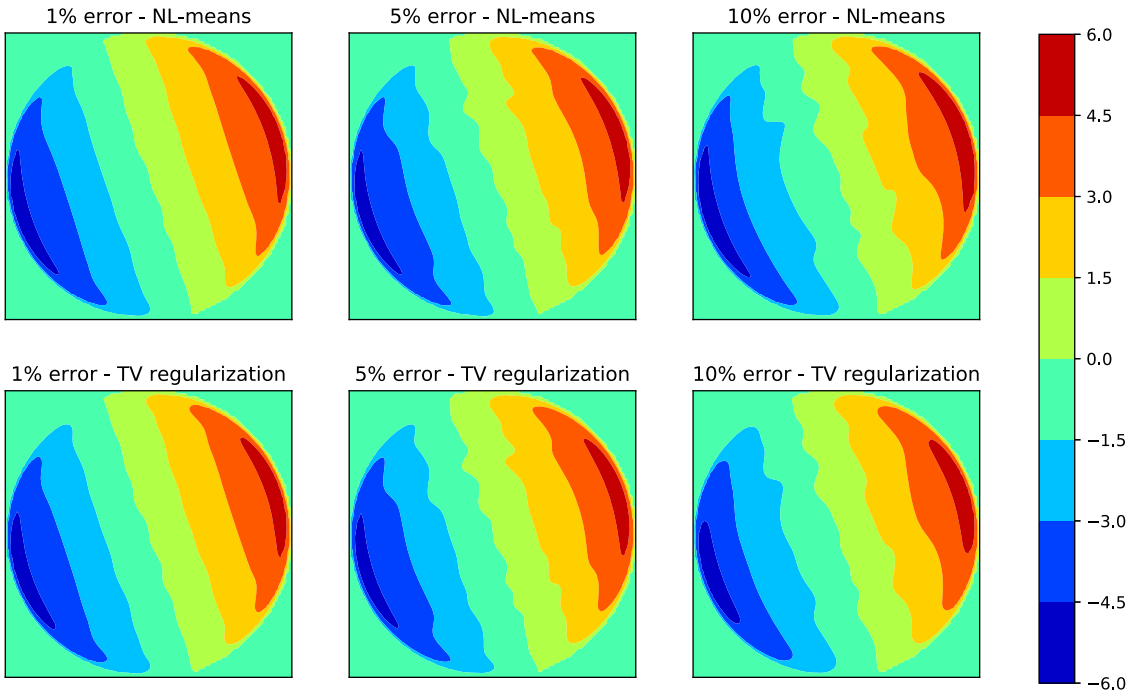

FIG. 6. Comparison between reconstructions of the asymmetric distribution represented by Eq. (12) obtained using the two path method with the 1%, 5%, and 10% error. Smoothing algorithms used in the process are NL-means (top row) and TV regularization (bottom row).

for each case: $\lambda = 0.1$ at 1% error, $\lambda = 0.5$ at 5% error, and $\lambda = 0.6$ at 10% error, the same as in the case of the Abel inversion technique. The difference between the reconstruction images was obtained quantitatively by employing the UQI and PSNR, which is shown in Table I. The values obtained in Table I show that the experimental data with 5% or less percentage error could be smoothed with either NL-means or TV regularization methods to obtain similar results, but for percentage errors higher than 5%, TV regularization methods should be used.

It should be noted that the two angle method is only useful when the distribution function possesses some limited symmetry, such as the distribution given by Eq. (12). In the case of fully asymmetric distribution functions, such as Eq. (13), observing the system at only two perpendicular angles will result in some information missing. Furthermore, the quality of the reconstruction highly depends on which two perpendicular angles are available for observation, as shown in Fig. 7. Figure 7 shows the comparison between the original function and its reconstruction when projections were taken at 0° and 90° and at 45° and 135° relative to the horizontal. No error was introduced. The universal image quality index was 0.69 and 0.68 for each set of projections, respectively, while the peak signal-to-noise ratio was 15.26 and 15.21. Even though, visually, the two images look very different, the quantitative analysis shows similar results for both.

TABLE I. Quality of the image reconstructed with the two angle approach by applying UQI and PSNR methods.

	NL-means		TV regularization	
	UQI	PSNR (dB)	UQI	PSNR (dB)
1% error	0.913	9.46	0.929	9.59
5% error	0.895	9.22	0.908	9.41
10% error	0.853	8.66	0.884	9.38

Clearly, for the systems with radial symmetry (such as the Gaussian distribution function), there is no need to employ the two angle approach since the internal structure of these systems can be reconstructed by employing the Abel inversion technique that requires only one observation direction. The above testing showed that *a priori* knowledge of the experimental system at hand is crucial when choosing the two angle approach.

C. Two dimensional tomography

In order to fully recover the desired information about the internal structure of the observed experimental system, the system should be observed at multiple angles in a half circle from 0° to 180°. A range of reconstruction algorithms have been developed and are available in the literature. The commonly used reconstruction algorithms fall under three families: analytical, algebraic, and statistical methods.

1. Analytical methods

The most common analytical method used nowadays is Filtered Back Projection (FBP).[26] The Filtered Back Projection technique is

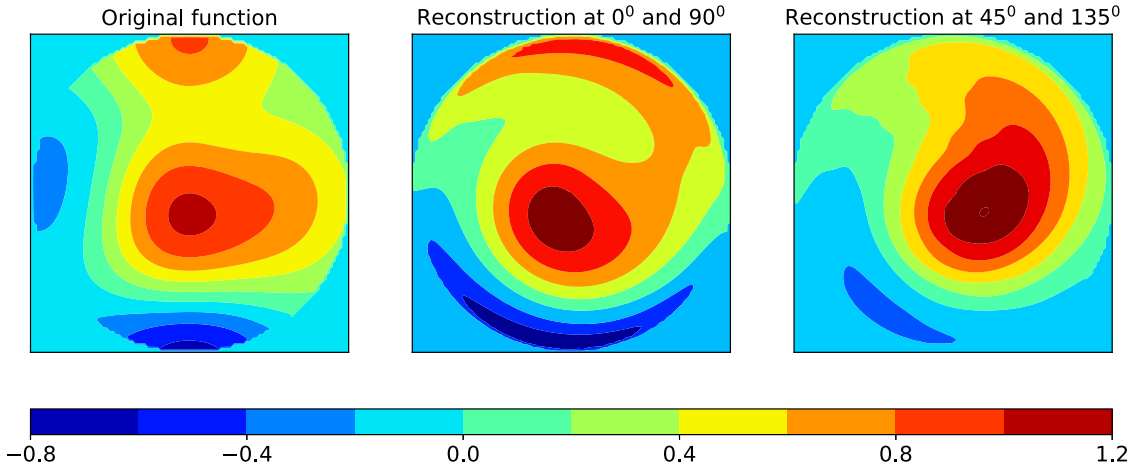

FIG. 7. Comparison between the original distribution, represented by Eq. (13), and its reconstruction obtained using the two path method when projections were taken at 0° and 90° (UQI = 0.69 and PSNR = 15.26) and at 45° and 135° relative to the horizontal (UQI = 0.68 and PSNR = 15.21).

based on solving the inverse Radon transform integral [Eq. (4)] by finding the Fourier transform of the distribution function $\varepsilon(x, y)$,

$$\varepsilon(x,y) = \int_{-\infty}^{\infty}\int_{-\infty}^{\infty} E(v_s, v_p)\exp[i2\pi(sv_s + pv_p)]\mathrm{d}v_s\mathrm{d}v_p. \quad (19)$$

Then, by applying the Fourier slice theorem,[20] the measured spectral line intensities can be expressed as a set of projections $I_\theta(p)$ for different angles θ, and the equation for the unknown spatial distribution function in polar coordinates becomes

$$\varepsilon(x,y) = \int_0^{\pi}\mathrm{d}\theta\int_{-\infty}^{\infty}\mathrm{d}v|v|F(I_\theta(p))\exp(i2\pi vp_0), \quad (20)$$

where $p_0 = sv_s + pv_p$.

In principle, the integration in the filtered projection given by Eq. (20) has to be carried over all frequencies. However, in practice, the energy contained in the Fourier transform components above a certain frequency is negligible, and we may consider the projections bandlimited. When the highest frequency in the projections is finite, Eq. (20) becomes

$$\varepsilon(x,y) = \int_0^{\pi}\mathrm{d}\theta\int_{-\infty}^{\infty}F(I_\theta(p))H(v)\exp(i2\pi vp_0)\mathrm{d}v, \quad (21)$$

where $H(v)$ is a high frequency noise filter.

Experimentally obtained line intensities are presented as a discrete set of projections, measured with the spatial sampling interval τ. Thus, $p = n\tau$, where n is an integer. If we assume that each projection $I_\theta(k\tau)$ is zero outside the index range $k = 0, 1, \ldots, K-1$, where K is the number of angles at which the projections are sampled, we may express the *filtered projection* as

$$\varepsilon(x,y) = \frac{\pi}{K}\sum_{i=1}^{K}\tau\sum_{k=0}^{K-1}h(n\tau - k\tau)I_\theta(k\tau), \quad n = 0,1,\ldots,K-1. \quad (22)$$

Here, we applied the inverse Fourier transform and the convolution theorem. This means that each filtered projection has to be back-projected.

In this work, we used the Shepp–Logan filter,[48] a commonly used filter in the literature,

$$h(n\tau) = \begin{cases} \dfrac{2}{\pi^2\tau^2}, & \mathrm{n} = 0 \\ -\dfrac{2}{n^2\pi^2(4v^2-1)}, & \mathrm{n} \neq 0. \end{cases} \quad (23)$$

Filtered Back Projection is an often employed reconstruction method because it is computationally very efficient and is already implemented in countless software packages.

Recently, another approach based on Fourier transform, named GRIDREC,[28,29] is developed. The algorithm for GRIDREC makes use of the gridding method for resampling the Fourier space from polar to Cartesian coordinates, offering both computational efficiency and negligible artifacts. The idea is to pass a convolution kernel $W(v_s, v_p)$ over the data sampled on the polar grid, with the convolutions' output evaluated at the points of the Cartesian grid. The contribution of $W(v_s, v_p)$ is then removed after the inverse Fourier transform. In polar coordinates, the convolution step can be expressed as follows:

$$\begin{aligned} H(v_s, v_p) &= F(v_s, v_p) * W(v_s, v_p) \\ &= \int_0^{\pi}\mathrm{d}\theta\int_{-\infty}^{\infty}\mathrm{d}v|v|F(I_\theta(p))W(v_s - v\cos\theta, v_p - v\sin\theta), \end{aligned} \quad (24)$$

where the multiplication $F(I_\theta(p))|v|$ in Eq. (24) corresponds to the filtering operation in FBP routines. As is the case of FBP, Eq. (24) needs to be discretized in order to implement the GRIDREC method. Consequently, computer implementation of tomographic reconstruction algorithms, based on both GRIDREC and FBP routines, can lead to several artifacts adversely affecting the reconstructed images as a result of the inherent discretization required.

2. Algebraic reconstruction techniques

The algebraic reconstruction techniques form a family of algorithms that aims at solving the tomographic problem iteratively.

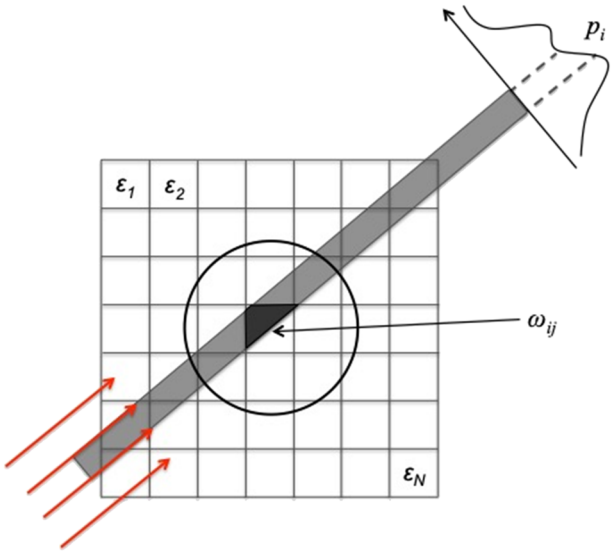

FIG. 8. Parallel beam projection scheme at a specific angle.

In these techniques, the distribution function to be reconstructed is modeled as a discrete array of pixels with an unknown value. The algorithm is based on altering the value of each pixel in such a way that their sum agrees with the values of the measured projections.[26]

Figure 8 shows a grid superimposed on the unknown distribution $\varepsilon(x, y)$. Let us assume that within each cell, the function $\varepsilon(x, y)$ is represented with ε_j and is uniform but different from other cells.

For algebraic techniques, the calculated projections, p_i, are represented with the finite width lines (rays) running through the (x, y)-plane. The calculated projection, p_i, is then the weighted sum of the rays that crossed the line of pixels in the distribution,

$$p_i = \sum_{j=1}^{N} w_{ij}\varepsilon_j, \quad i = 1, 2, \ldots M, \tag{25}$$

where M is the total number of rays (in all the projections), N is the total number of cells, and w_{ij} is the weighting factor that represents the contribution of the jth cell to the ith ray integral. Algebraic reconstruction techniques are iterative techniques. After q iterations, the calculated projection, $p_i^{(q)}$, is compared to the measured projection, I_i, and the values of the unknown distribution, $\varepsilon_j^{(q)}$, are updated as

$$\varepsilon_j^{(q)} = \varepsilon_j^{(q-1)} + w_{ij}\frac{I_i - p_i^{(q)}}{\sum_{j=1}^{N} w_{ij}^2}, \tag{26}$$

with initial values chosen as $\varepsilon_j^{(0)} = 0$.

Various computer implementations were developed for algebraic reconstruction techniques. In this study, we will discuss the application of the Algebraic Reconstruction Technique (ART) and Simultaneous Algebraic Reconstruction Technique (SIRT) for tomography purposes. In both of these methods, w_{ij}'s in Eq. (26) are simply replaced by ones and zeroes, depending upon whether the center of the jth image cell is within the ith ray. In this case, the number of pixels under projection ray p_i is defined as $N_i = \sum_{j=1}^{N} w_{ij}^2$. The approximations used for w_{ij}'s lead to the poor agreement between the computed projections p_i and measured projections I_i. Furthermore, in ART implementation, the value of the cell ε_j is changed every time a computed projection ray passes through it, thus increasing inconsistencies between the measured and calculated projections. This problem is solved in the SIRT algorithm by changing the value of ε_j after all the equations are performed and taking the average value of all the changes proposed in each step.

3. Statistical reconstruction methods

The main idea behind the statistical methods is to incorporate the counting statistics of the detected particles into the reconstruction process.[31,32] This means that the detected intensity of particles (measured projection) will become a random variable.

Statistical reconstruction methods are a very useful tool in cases where the signal-to-noise ratio of the reconstructed image plays

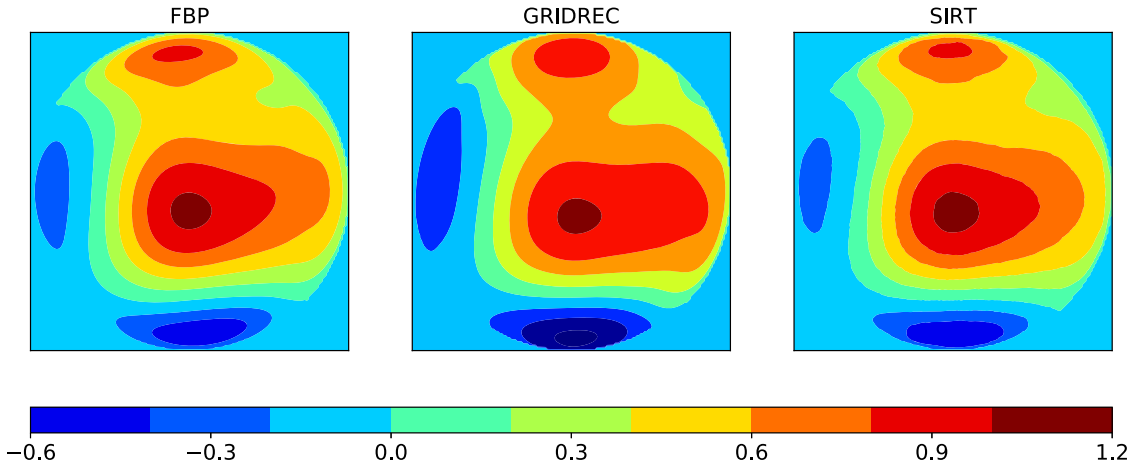

FIG. 9. Comparison between reconstructions of the asymmetric distribution [Eq. (13)] obtained with FBP, GRIDREC, and SIRT tomography methods.

TABLE II. Quality of the image reconstructed using FBP, GRIDREC, and SIRT approaches with no, 1%, 5%, and 10% random noise on the 0°–180° range of angles.

	FBP		GRIDREC		SIRT	
	UQI	PSNR (dB)	UQI	PSNR (dB)	UQI	PSNR (dB)
No error	0.862	24.50	0.831	23.9	0.874	27.35
1% error	0.814	24.35	0.831	23.88	0.873	27.31
5% error	0.803	24.27	0.823	23.82	0.870	27.22
10% error	0.801	24.07	0.816	23.87	0.864	26.88

the most important role, i.e., medical image reconstructions. However, in emission plasma tomography based on optical emission spectroscopy, the reconstructed distribution function represents the population densities of the various plasma species. Therefore, it is crucial to reconstruct the absolute values of the unknown distribution, thus making these approaches not optimal for the purposes of this study.

4. Testing results

Python module TomoPy was implemented to employ GRIDREC, ART, and SIRT algorithms, while the algorithm for FBP was written by the authors. The algorithms were tested on the asymmetric distribution function given with Eq. (13). As expected, with a sufficiently large number of observed angles and projections, employing any of the methods resulted in a high quality reconstructed image (UQI between 0.93 and 0.98 and PSNR = 33–38 dB). However, a large number of viewing angles and projections are not often available under experimental conditions. Specifically, in the experimental setup used for testing the reconstruction methods, reconstructions were calculated at only 17 projections at 21 angles. Thus, to simulate the data obtained in the experimental setup, we tested the quality of reconstruction techniques at exactly 17 projections and 21 angles. The angles were first generated on the 0°–180° interval.

Since ART and SIRT algorithms are very similar and SIRT showed better results during testing, only the images reconstructed using the SIRT algorithm are presented in this paper. Figure 9 shows the comparison between the applied methods when there was no error introduced to the system. By visual inspection of Fig. 9, it is very hard to determine which reconstruction matches the original image the best. We tested the quality of the reconstructed images with two quantitative methods, UQI and PSNR. Additionally, the image quality of the results reconstructed when a random noise of 1%, 5%, and 10% is added is presented in Table II. All results were denoised by employing the total variation minimization denoising method that proved to be the best denoising technique. The regularization parameter was 0.01, 0.05, and 3 for FBP, SIRT, and GRIDREC, respectively. Even though the UQI of FBP is comparable to the UQI of the SIRT method, when no error is introduced to the system (see Table II), the PSNR shows that better matching is obtained by applying the SIRT algorithm. As given in Table II, when the error is introduced to the system, the best results are obtained from the SIRT algorithm.

As the last step in testing, we have addressed the problem of a limited range of measured angles. In our experiment, it was not possible to approach the plasma from every angle. We were able to collect data only on the 48°–168° interval. Thus, we tested the algorithms on this exact range of angles. We used the cubic spline fit to

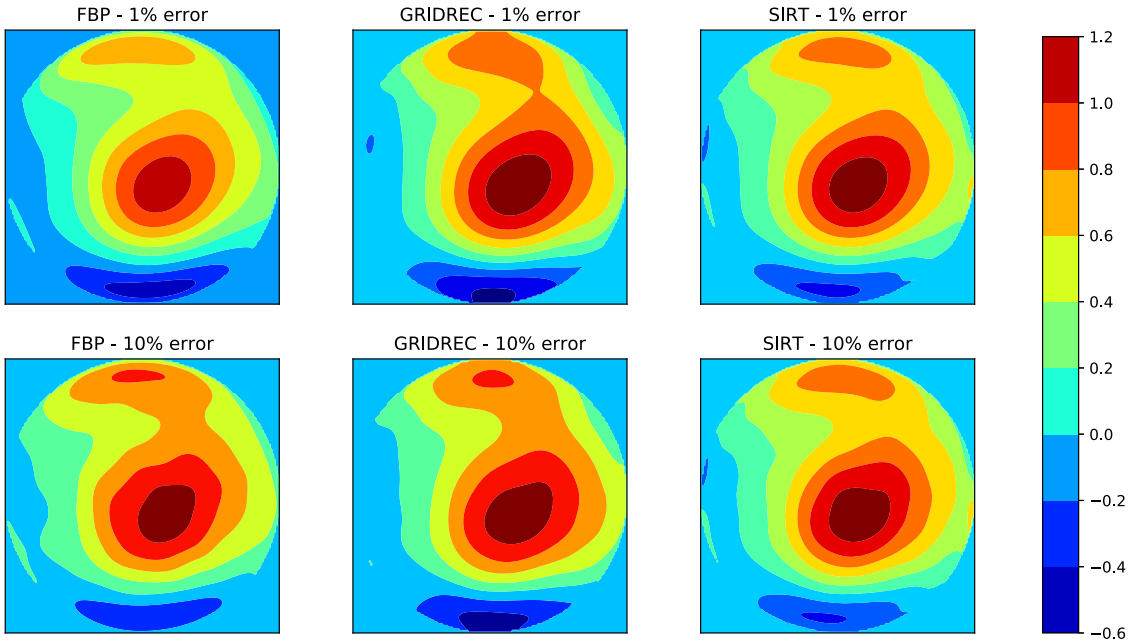

FIG. 10. Comparison between the reconstructions (FBP, GRIDREC, and SIRT) of the distribution function given by Eq. (13) with the 1% and 10% error.

TABLE III. Quality of the image reconstructed using FBP, GRIDREC, and SIRT approaches with 1%, 5%, and 10% random noise on the 48°–168° range of angles.

	FBP		GRIDREC		SIRT	
	UQI	PSNR (dB)	UQI	PSNR (dB)	PSNR	PSNR (dB)
1% error	0.777	19.13	0.765	20.01	0.758	20.21
5% error	0.755	19.17	0.761	20.06	0.758	20.18
10% error	0.727	19.16	0.760	20.14	0.758	20.15

extrapolate the missing data. All results were denoised by employing the total variation minimization denoising method that proved to be the best denoising technique. The regularization parameter was 0.01, 3, and 3 for FBP, SIRT, and GRIDREC, respectively. The effects of the percentage error on the reconstructed test function are presented in Fig. 10. As expected, missing and noisy data did result in a poorer tomographic reconstruction. Even with the use of the spline extrapolation of the data, Fig. 10 shows that the areas with missing data were reconstructed as zero values. The quantitative values of the reconstructed image quality are presented in Table III. Table III shows an interesting fact that the UQI and PSNR had very similar values for all three applied algorithms. Even though the iterative technique, SIRT, and the algebraic technique, GRIDREC, possess slightly better UQI and PSNR values than FBP, both methods required a very large regularization parameter of three in order to achieve comparable results as FBP. The disadvantage is that using a very large regularization parameter in tomographic reconstruction may result in losing some useful information about the reconstructed image.

We can conclude that in the case when the data are sparse (17 projections at 21 angles), at limited range (48°–168° angle interval), and noisy, using any of the three approaches would result in a similar reconstruction image that should be taken with great caution.

VI. EXPERIMENTAL RESULTS

The proposed inversion techniques were used to analyze the experimental data obtained in a supersonic flowing tube in combination with the microwave cavity discharge, shown in Fig. 11. The discharge was generated inside a cylindrical quartz tube with the inner diameter of 32 mm. The working pressure in the evacuated quartz tube was kept between 1 Torr and 3 Torr. A Mach 2, cylindrical convergent–divergent De Laval nozzle was used to sustain the supersonic flowing discharge downstream of the microwave cavity, which operated in the TE_{111} mode. The measurements were performed in pure argon. A detailed explanation of the experimental setup is given in Ref. 43.

In the afterglow of the MW supersonic flow region, we observed a plasmoid-like formation as a secondary downstream phenomenon coupled to the microwave cavity. The plasmoid appears to be sustained by a low power surface wave, which propagates along its surface and the surface of the quartz tube. Our initial analysis led to the conclusion that plasmoid formation may be caused by aerodynamic effects in the supersonic flow. The full interpretation of the plasmoid discharge requires knowledge of all effects causing its formation. For that reason, we calculated spatial population distributions of the neutral Ar excited state $\left[3s^2 3p^5 (^2P^0_{1/2}) 4p, J = 1\right]$.

We employed optical emission spectroscopy as a diagnostic tool to observe the spectra of the Ar excited states. Emission spectra were recorded using an imaging spectrograph (Acton SpectraPro) connected to the charged-coupled device (CCD) camera (Apogee, Hamamatsu, Back-Illum). All spectral measurements were performed side-on with respect to the direction of the discharge flow. In order to increase the precision of experimental measurements, we have built an automated measurement system (AMS). It consists of a flat mirror and a set of feedback sensors connected to two high-precision stepper motors driven by a microcontroller-based system, as shown in Fig. 12. As shown in Fig. 12, instead of rotating the detecting system around the plasma, we set the detecting system at the fixed position and collected light emitted from the plasma at different angles by using a rotating mirror. This was achieved by applying the simple rules of trigonometry, as shown in Fig. 13. The details on AMS can be found in Ref. 43. The observed spectra were calibrated using a Newport/Oriel absolute black body irradiance source. The calibration graphs were taken under the same conditions and by repeating the same geometry of the experiment as the experimental data. We evaluated the calibration graphs of

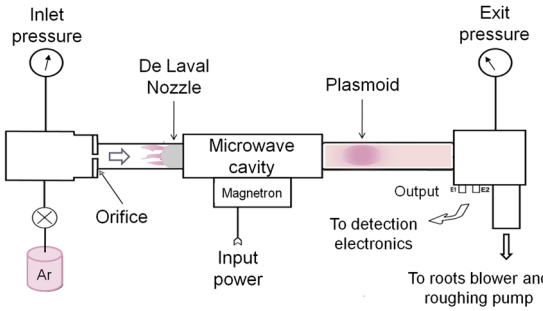

FIG. 11. Scheme of the supersonic flowing microwave discharge. Reprinted with permission from M. Nikolic, "Characterization of microwave discharge plasmas for surface processing," Ph.D. dissertation (Old Dominion University, 2013).[43]

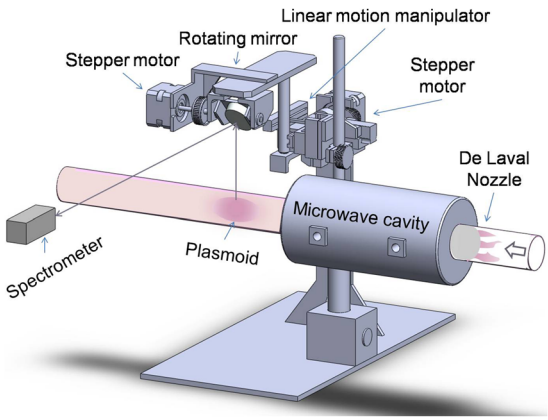

FIG. 12. Schematic of the automated measurement system. Reprinted with permission from M. Nikolic, "Characterization of microwave discharge plasmas for surface processing," Ph.D. dissertation (Old Dominion University, 2013).[43]

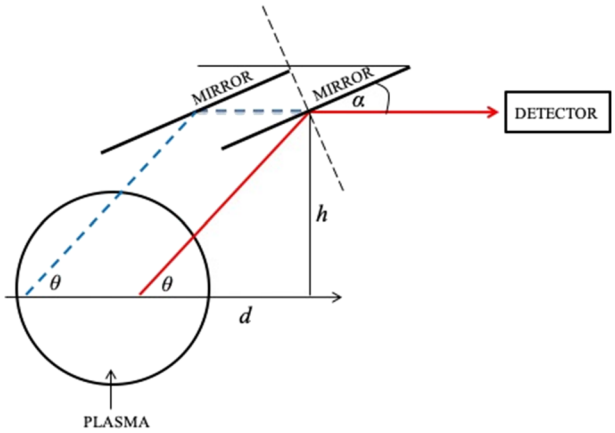

FIG. 13. Schematic of a setup used for spatial measurements at a given angle θ and two different projections.

spectral irradiance per count vs wavelength for wavelengths between 500 and 1100 nm. Using these graphs, we determined the population densities of the upper energy levels of particular Ar excited state transitions. A detailed procedure of how this was done is given in Ref. 43. By using a standard back reflector procedure, we eliminated the possibility that the optical thickness of the measured spectral line intensity was interfering with our measurement.[44] All spectral line intensities were higher by a factor of two in comparison to the direct plasma observation.[43] Therefore, we assumed that the plasma was optically thin, and the radiation trapping along the observation path could be neglected. In the case of the optically thin plasma, the spectral line intensity is proportional to the number of atoms populating the higher energy level. An example of the optical emission spectra used for data analysis is given in Fig. 14.

Based on the cylindrical geometry of the experimental system, we assumed that the plasma would be radially symmetric too. This meant that it would be sufficient to obtain projections at only one

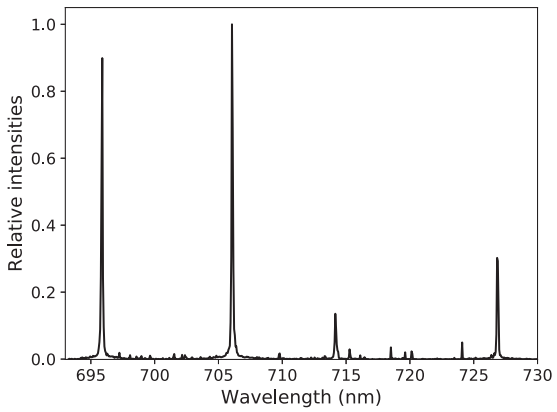

FIG. 14. Example of the optical emission spectroscopy measurement. Data are taken in pure argon at 2.4 mTorr.

angle and then to perform Abel inversion. However, due to the turbulent flow downstream of the supersonic region, it was possible that the plasmoid-like formation did not possess radial symmetry. For that reason, we first observed the plasmoid at three different angles and performed Abel inversion at each angle. Figure 15 shows the spatial distributions of population densities of the Ar I $\left[3s^2 3p^5 (^2P^0_{1/2}) 4p, J = 1\right]$ state obtained from the spectral line intensity at 714.70 nm after applying the Abel inversion integral taken at distance 3 cm from the cavity at three different angles: 48°, 138°, and 90°. It can be deduced from Fig. 15 that since reconstructions differ from each other, the plasmoid-like formation did not possess radial symmetry. Thus, Abel inversion would not be a good choice as the reconstruction technique. However, all three reconstructed distributions showed very similar trend, indicating that, possibly, spatial distributions of Ar I energy levels deviate only slightly from radial symmetry. Hence, reconstructing the spatial distributions of Ar I states, using a two angle approach described in Subsection V B, could result in quality reconstruction of the internal plasma states.

We applied the two angle approach to obtain spatial distribution of Ar I excited states at 714.70 nm. The populations were evaluated at three different positions across the plasmoid relative to the cavity. The first measurements were taken 3 cm from the cavity corresponding to the beginning of the plasmoid. The next position measured was at 4.5 cm from the cavity that corresponds to the middle range of the plasmoid. Finally, we observed the end of the plasmoid by taking measurements 8 cm from the cavity. All data were smoothed by applying the TV-regularization method with the regularization parameter, λ, of 0.5.

Figure 16 shows how the spatial distribution of Ar I excited states at 714.70 nm is changing along the plasmoid when the two angle approach was employed. It could be seen from the figure that the argon atoms are mainly populated close to the inner surface of the quartz tube, specifically at only one side of the quartz tube. This could indicate the turbulent behavior of the discharge, which could be described only when time-resolved diagnostic methods are applied. The maximal value population density reaches at the surface of the tube is $N = 1.6 \times 10^5$ cm^{-3}.

As a final test, we applied full 2D tomography to obtain spatial distributions of the excited Ar I $\left[3s^2 3p^5 (^2P^0_{1/2}) 4p, J = 1\right]$ state obtained from the spectral line intensity at 714.70 nm. Similarly, as in the above work, all results were smoothed by applying the TV-regularization method. The regularization parameter was 0.01, 3, and 3 for FBP, SIRT, and GRIDREC, respectively. The results from the three reconstruction techniques tested in Sec. V C 4 are presented in Fig. 17.

It is shown in Fig. 17 that similar results are obtained; argon atoms are distributed mostly at the inner surface of the tube. The maximal population density was $N = 1.3 \times 10^5$ cm^{-3} for FBP, $N = 1.5 \times 10^5$ cm^{-3} for SIRT, and $N = 1.5 \times 10^5$ cm^{-3} for the GRIDREC technique, which is in good agreement with the results obtained by employing the two angle method.

Even though reconstructed spatial distributions from SIRT and GRIDREC compare better visually to the two angle approach reconstructions (Fig. 16) and had a slightly better PSNR for the testing function [Eq. (13)], a large regularization parameter used for denoising may have caused the loss of some valuable information. Therefore, we have chosen to use the FBP technique to reconstruct spatial distributions of the excited Ar I state at 714.70 nm since it

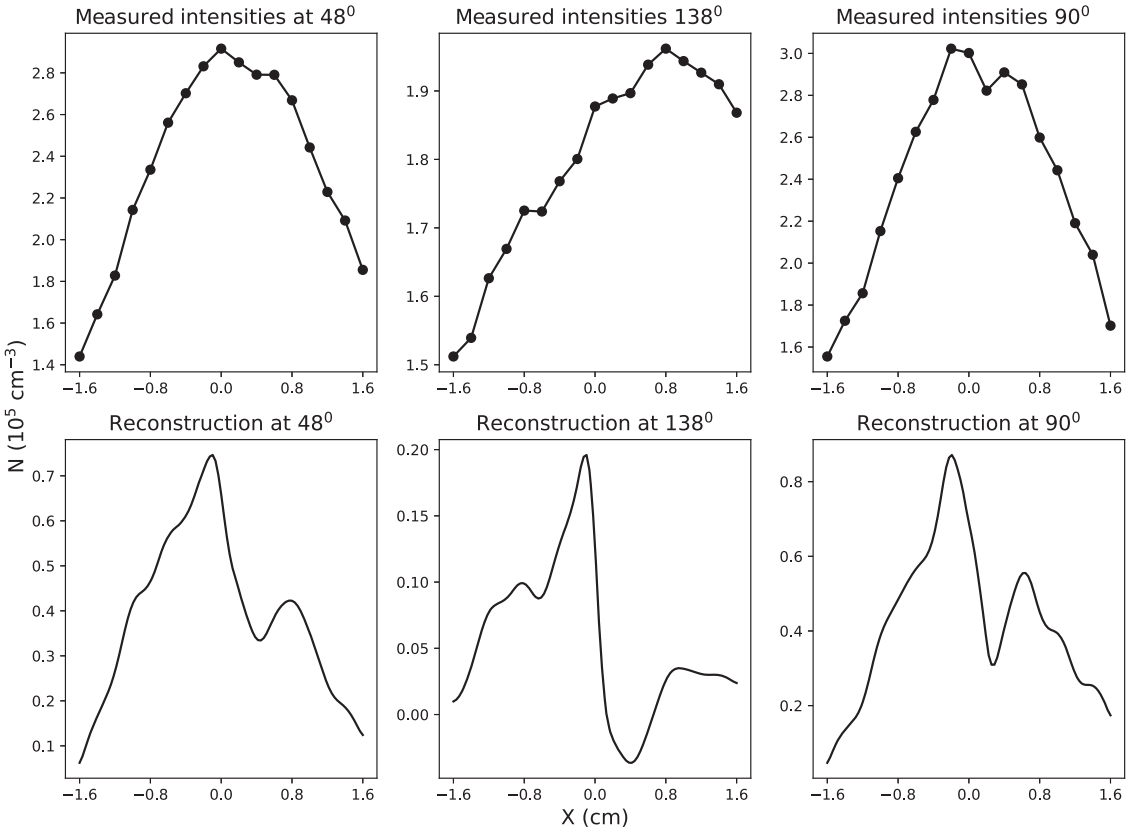

FIG. 15. Calibrated measured spectral line intensities (top row) and spatial distributions (bottom row) of Ar I $\left[3s^2 3p^5 (^2P^0_{1/2}) 4p, J = 1\right]$ population density obtained by applying the Abel inversion integral taken at distance 3 cm from the cavity.

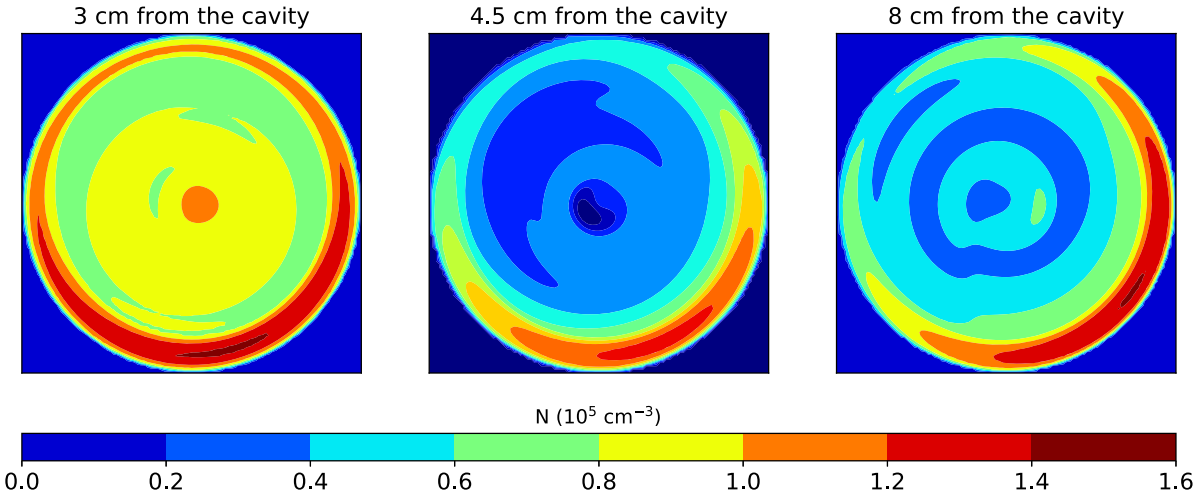

FIG. 16. Spatial distributions of the Ar I $\left[3s^2 3p^5 (^2P^0_{1/2}) 4p, J = 1\right]$ population density obtained using the two angle approach at distances of 3 cm, 4.5 cm, and 8 cm from the cavity.

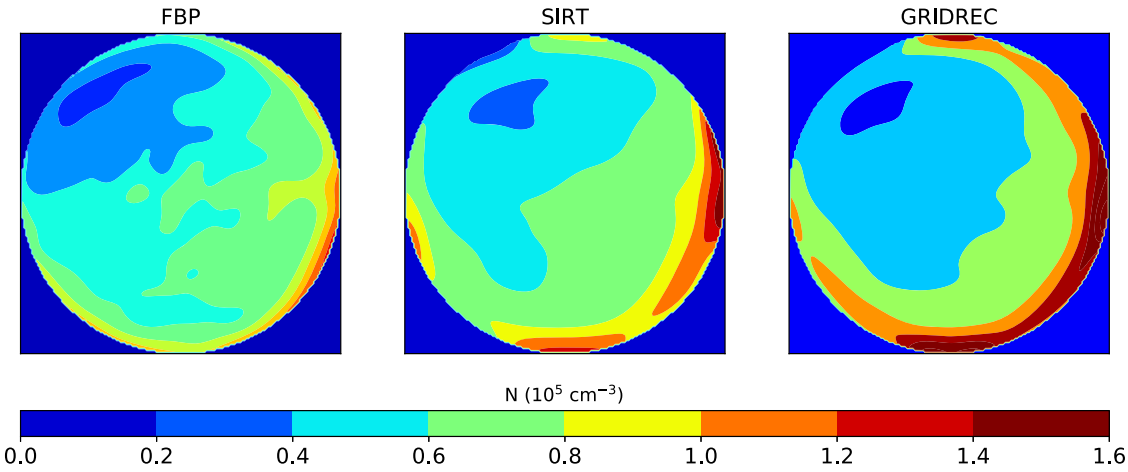

FIG. 17. Spatial distributions of Ar I $\left[3s^2 3p^5 (^2P^0_{1/2}) 4p, J = 1\right]$ population density obtained by FBP, SIRT, and GRIDREC algorithms, respectively, measured at distance 3 cm from the cavity.

offers similar quality reconstructions with a very small regularization parameter $\lambda = 0.01$ even for very noisy and sparse data.

Figure 18 presents spatial distributions of the excited Ar I state at 714.70 nm at three different positions across the plasmoid relative to the cavity: 3 cm from the cavity (at the beginning of the plasmoid), 4.5 cm from the cavity (in the middle of the plasmoid), and 8 cm away from the cavity (at the end of the plasmoid). It is evident that at each position, argon atoms are mainly populated close to the inner surface and that the plasmoid-like formation is sustained by a surface wave.

The lack of cylindrical symmetry in the distributions of population densities could be attributed to two factors: our ability to measure at a limited range of angles (48°–168°) and the possibility that the supersonic microwave discharge was driven mainly by the turbulent flow. To test the validity of the first statement, we simulated experimental conditions on the symmetric Gaussian distribution function. When we applied the cubic spline extrapolation function to extend the viewing angle range, we were able to completely reconstruct the original function. Therefore, we can conclude that the internal structure of the plasmoid-like formation in the afterglow of the MW supersonic plasma varies constantly due to the turbulent flow in the supersonic region. To fully understand the effects of aerodynamics on the supersonic plasma flow, it would be beneficial to observe the plasmoid formation in the time-resolved regime.

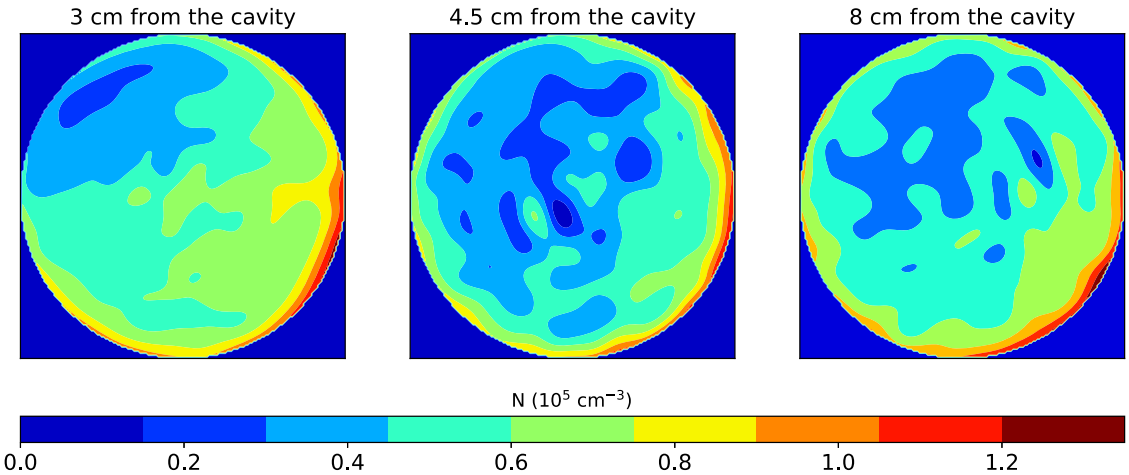

FIG. 18. Spatial distributions of Ar I $\left[3s^2 3p^5 (^2P^0_{1/2}) 4p, J = 1\right]$ population density obtained using the FBP algorithm with the Shepp–Logan filter measured at distances 3 cm, 4.5 cm, and 8 cm from the cavity.

The details on how the spatially averaged population densities of the excited argon states are changing in time could be found in Ref. 49.

From the data analysis, we can conclude that in the case of the supersonic microwave discharge experiment that is highly affected by the turbulent flow, the full two-dimensional tomography algorithms provide more reliable reconstructions of the internal plasma structure. When the number of viewing angles at the given experimental system at hand is limited and it is impossible to employ full, 2D plasma tomography, we recommend applying the two angle approach to obtain at least a qualitative insight into the spatial distributions of the plasma constituents.

VII. CONCLUSION

Various tomographic reconstruction methods and image denoising techniques were employed and tested in order to choose the best approach to study the internal plasma structure for the experiment at hand. The reliability and performance of the developed reconstruction methods were demonstrated for the case of the experimental setup of the supersonic flowing argon MW discharge sustained inside the cylindrical quartz tube. The analysis was focused on the afterglow region of the MW flow where a plasmoid-like formation was observed.

The application of the tomographic methods was tested with three different functions chosen in such a way to simulate various experimental setups: one that possesses radial symmetry, one possessing slight radial asymmetry, and one with an asymmetric function. A random noise between 1% and 10% was added to each function to mimic the error in the experimental data. The quality of reconstructed images was obtained by two methods: universal image quality index and signal-to-noise ratio. It was shown that in order to smooth and denoise the data, the best results were obtained when using the total variation minimization method. To deduce the type of symmetry of the experimental data, the inverse Abel integral at one angle should be performed. In the case of radial symmetry, high quality reconstructions could be obtained by employing Abel inversion at only one angle. Slightly asymmetric data could be reconstructed by applying the two angle approach where data were obtained at two mutually perpendicular angles. Finally, in the complete absence of radial symmetry, full 2D tomographic reconstruction should be applied. The data analysis showed that the best results were obtained by employing either the analytical method, filtered back projection, or the simultaneous Algebraic reconstruction technique.

Each tomographic approach (Abel inversion, two angle approach, and 2D tomography) was applied to obtain the spatial distributions of the Ar I excited state $\left[3s^2 3p^5 (^2P^0_{1/2}) 4p, J = 1\right]$ observed at 714.7 nm in the supersonic flowing MW discharge experiment. Spectral measurements were taken at three different positions along the plasmoid-like structure by employing optical emission spectroscopy. The results from all three approaches indicated the lack of radial symmetry of the plasma constituents, meaning that the discharge was highly affected by the turbulent supersonic flow and should be reconstructed by either the two angle approach or the 2D tomography. Both approaches showed similar results; argon atoms were mainly populated close to the inner surface of the quartz tube at only one side of the quartz tube, indicating that the discharge is probably sustained by a surface wave that varies with the turbulent flow. Finally, the full 2D tomography FBP technique in combination with the TV-regularization denoising method was chosen as the best reconstruction technique in this case due to its high-quality reconstruction with a very small regularization parameter $\lambda = 0.01$, even for very noisy and sparse data.

REFERENCES

[1] M. A. Lieberman and A. J. Lichtenberg, *Principles of Plasma Discharges and Materials Processing*, 2nd ed. (John Wiley & Sons, Inc., New York, 2005).
[2] J. W. Coburn, R. A. Gottscho, and D. W. Hess, *Plasma Processing* (Material Research Society, Pittsburgh, 1986).
[3] F. F. Chen, *Plasma Diagnostic Techniques*, edited by R. H. Huddlestone and S. L. Leonhard (Academic, New York, 1965).
[4] R. Hippler, S. Pfau, M. Schmidt, and K. H. Schoenbach, *Low Temperature Plasma Physics* (Wiley, Berlin, 2001).
[5] I. H. Hutchinson, *Principles of Plasma Diagnostics* (Cambridge University Press, Cambridge, 1987).
[6] O. Auciello and D. C. Flamm, *Plasma Diagnostics* (Academic, San Diego, 1989), Vol. 1.
[7] V. M. Donnelly, J. Phys. D: Appl. Phys. **37**, R217 (2014).
[8] X.-M. Zhu and Y.-K. Pu, J. Phys. D: Appl. Phys. **40**, 2533 (2007).
[9] D. Mariotti, Y. Shimizu, T. Sasaki, and N. Koshizaki, Appl. Phys. Lett. **89**, 201502 (2006).
[10] S. Wang, A. E. Wendt, J. B. Boffard, C. C. Lin, S. Radovanov, and H. Persing, J. Vac. Sci. Technol., A **31**, 021303 (2013).
[11] J. B. Boffard, R. O. Jung, C. C. Lin, and A. E. Wendt, Plasma Sources Sci. Technol. **18**, 035017 (2009).
[12] J. Li, F.-X. Liu, X.-M. Zhu, and Y.-K. Pu, J. Phys. D: Appl. Phys. **44**, 292001 (2011).
[13] R. Álvarez, A. Rodero, and M. C. Quintero, Spectrochm. Acta, Part B **57**, 1665 (2002).
[14] J. R. Roberts, J. Res. Natl. Inst. Stand. Technol. **100**, 353 (1995).
[15] R. Rompe and M. Steinbeck, *Progress in Plasmas and Gas Electronics* (Academie-Verlag, Berlin, 1975), Vol. 1.
[16] W. L. Barr, J. Opt. Soc. Am. **52**, 885 (1962).
[17] M. M. Prost, Spectrochim. Acta Part B **37**, 541 (1982).
[18] A. Okigawa, T. Makabe, T. Shibagaki, N. Nakano, Z. Petrovic, T. Kogawa, and A. Itoh, Jpn. J. Appl. Phys., Part 1 **35**, 1890 (1996).
[19] J. Radon, IEEE Trans. Med. Imaging **5**, 170 (1986).
[20] V. V. Pikalov, *Plasma Tomography* (Nauka, Novosibirsk, 1995).
[21] F. Naterer, *The Mathematics of Computerized Tomography* (Wiley, New York, 1996).
[22] G. Khermen, *Image Reconstruction from Projections, The Fundamentals of Computerized Tomography* (Academic, New York, London, 1980).
[23] A. Okigawa, M. Tadokoro, A. Itoh, N. Nakano, Z. Lj. Petrović, and T. Makabe, Jpn. J. Appl. Phys., Part 1 **36**, 4605 (1997).
[24] M. P. Freeman and S. Katz, J. Opt. Soc. Am. **53**, 1172 (1963).
[25] K. G. Lapworth and L. A. Allnutt, J. Phys. E: J. Sci. Instrum. **10**, 727 (1977).
[26] M. Slaney and A. Kak, *Principles of Computerized Tomographic Imaging* (Society for Industrial and Applied Mathematics, Philadelphia, 1988).
[27] Y. Miyoshi *et al.*, J. Phys. D: Appl. Phys. **35**, 454 (2002).
[28] B. A. Dowd, G. H. Campbell, R. B. Marr, V. Nagarkar, S. Tipnis, L. Axe, and D. P. Siddons, Proc. SPIE **3772**, 224 (1999).
[29] F. Marone and M. Stampanoni, J. Synchrotron Radiat. **19**, 1029 (2012).
[30] R. Gordon, R. Bender, and G. T. Herman, J. Theor. Biol. **29**, 471 (1970).
[31] J. A. Fessler, *Handbook of Medical Image Processing and Analysis* (SPIE Press, 2000), Vol. 2, Chap. 1.
[32] A. J. Rockmore and A. Macovski, IEEE Trans. Nucl. Sci. **24**, 1929 (1977).
[33] S. W. Smith, *Moving Average Filters in Digital Signal Processing*, edited by S. W. Smith (Newnes, 2003), Chap. 15.

[34]A. Buades, B. Coll, and J.-M. Morel, "A non-local algorithm for image denoising," in *2005 IEEE Computer Society Conference on Computer Vision and Pattern Recognition (CVPR'05)* (IEEE, 2005), Vol. 10, No. 2.
[35]N. He and K. Lu, *Images Denoising by Improved Non-Local Means Algorithm in Theoretical and Mathematical Foundations of Computer Science*, edited by Q. Zhou (Springer Berlin Heidelberg, 2011).
[36]J. Duran, B. Coll, and C. Sbert, Image Process. Line **3**, 311 (2013).
[37]A. Chambolle, V. Duval, G. Peyré, and C. Poon, J. Phys.: Conf. Ser. **756**, 012007 (2016).
[38]A. N. Tikhonov, "Solution of incorrectly formulated problems and the regularization method," Sov. Math. Dokl. **4**, 1035–1038 (1963).
[39]A. Tikhonov and W. J. Arsenine, *Solutions of Ill Posed Problems* (Winston; Wiley, Washington DC, 1977).
[40]M. Salewski *et al.*, Nucl. Fusion **56**, 106024 (2016).
[41]A. S. Jacobsen *et al.*, Plasma Phys. Control. Fusion **58**, 045016 (2016).
[42]Z. Wang and A. C. Bovik, IEEE Sig. Process. Lett. **9**, 81 (2002).
[43]M. Nikolić, Ph.D. dissertation (Old Dominion University, 2013).
[44]B. Bachmann *et al.*, J. Phys. D: Appl. Phys. **46**, 125203 (2013).
[45]T. N. Pappas and R. J. Safranek, *Perceptual Criteria for Image Quality Evaluation in Handbook of Image and Video Processing*, edited by A. C. Bovik (Academic Press, 2000).
[46]L. Fan, F. Zhang, H. Fan, and C. Zhang, Vis. Comput. Ind. Biomed. Art **2**, 7 (2019).
[47]C. Sutour, C. A. Deledalle, and J. F. Aujol, IEEE Trans. Image. Process. **23**, 8 (2014).
[48]L. A. Shepp and B. F. Logan, IEEE. Trans. Nucl. Sci. **21**, 21 (1974).
[49]M. Nikolić, J. Newton, C. I. Sukenik, L. Vušković, and S. Popović, J. Appl. Phys. **117**, 023304 (2015).